Large eddy simulation studies of two-phase flow characteristics in the abrasive flow machining of complex flow ways with a cross-section of cycloidal lobes

Junye Li, Tuo Sui and Xiwei Dong

School of Electromechanical Engineering,
Changchun University of Science and Technology,
Changchun, 130022, Jilin, China
Email: ljy@cust.edu.cn
Email: suituogege@163.com
Email: 2224556058@qq.com

Fengshou Gu

Centre for Efficiency and Performance Engineering,
University of Huddersfield,
Queensgate, Huddersfield, West Yorkshire, HD1-3DH, UK
Email: f.gu@hud.ac.uk

Ningning Su, Jianhe Liu* and Chengyu Xu

School of Electromechanical Engineering,
Changchun University of Science and Technology,
Changchun, 130022, Jilin, China
Email: 1497116870@qq.com
Email: ljhmach@163.com
Email: zhusf1497116870@163.com
*Corresponding author

Abstract: To accurately analysis and improve the performance of abrasive flow machining (AFM) in machining complex and special-shaped channel-parts, this study carried on a digital twin analysis, integrated with numerical and experimental approaches of cycloid special-shaped inner curved workpieces. The different sub-grid models are analysed and compared through large eddy simulation (LES), and the influence of processing factors is explored via the simulation and verified through experiments. The numerical results show that the dynamic kinetic energy sub-grid scale model can reflect the turbulent characteristics in the channel more accurately. The orthogonal test results show that the workpiece surface quality under AFM is greatly improved, and the surface roughness is reduced from 1.635 μm to 0.305 μm under the best combination of processing parameters. It reveals the fundamental behaviour of surface material removal and provide basis for the AFM processing of the special-shaped inner surface polished.

Keywords: special-shaped inner curved; large eddy simulation; LES; sub-grid model; surface roughness.

Reference to this paper should be made as follows: Li, J., Sui, T., Dong, X., Gu, F., Su, N., Liu, J. and Xu, C. (2022) 'Large eddy simulation studies of two-phase flow characteristics in the abrasive flow machining of complex flow ways with a cross-section of cycloidal lobes', *Int. J. Hydromechatronics*, Vol. 5, No. 2, pp.136–166.

Biographical notes: Junye Li is a Professor of Changchun University of Science and Technology. He has been engaged in teaching and scientific research in the fields of mechanical manufacturing technology and equipment, fluid transmission and control, precision and ultra-precision machining technology for a long time. He is a senior member of the Chinese Mechanical Engineering Society, and also serves as a young editor and reviewer for several journals.

Tuo Sui is a graduate student at Changchun University of Science and Technology, and took part in engineering projects, particularly works in simulation.

Xiwei Dong is a graduate student at Changchun University of Science and Technology. During the postgraduate period, he published an SCI paper and won the National Inspirational Scholarship once.

Fengshou Gu is a Professor of Machine Diagnostics at University of Huddersfield (UoH), and he is the Deputy Director of the Centre for Efficiency and Performance Engineering (CEPE) and the Head of Measurement and Data Analysis Research Group (MDARG) at CEPE. He has worked in the field of machine monitoring and diagnostic for more than 30 years in developing an advanced diagnostic laboratory and numerical simulation methods which have facilities to simulate various faults for majority machines.

Ningning Su graduated from Changchun University of Science and Technology. During the postgraduate period, published many papers.

Jianhe Liu graduated from Changchun University of Science and Technology in 2000, majoring in Mechanical Manufacturing Technology and Equipment, with a Bachelors degree. He graduated from Changchun University of Science and Technology in 2003, with a Masters degree majoring in Mechanical Manufacturing and Automation. He was named an assistant researcher in 2003 and a researcher in 2014.

Chengyu Xu is currently a Lecturer in the Department of Mechanical Design, Manufacturing and Automation, Changchun University of Science and Technology. He presided over or participated in six national, provincial and ministerial scientific research projects, published two papers included in SCI, one paper included in EI, eight Chinese core papers, seven authorised invention patents, one utility model patent, and outstanding achievements.

1 Introduction

The rapid development of modern engineering technology puts forward higher requirements for product quality, but the problem of small burrs or scratches on complex and special-shaped workpiece surfaces has not been solved effectively. Traditional

machining process is applicable to simple geometric shapes but is not suitable for complex geometric shapes and profiles. Abrasive flow machining (AFM) technology is not limited to the shape and size of the workpiece and can achieve good polishing effects on parts such as micro holes, irregular holes, complex internal cavity structures and uneven surfaces (Sambharia and Mali, 2019; Kum et al., 2020; Mali and Manna, 2009; Cheema et al., 2012). Its working principle is to squeeze the abrasive fluid with special rheological characteristics to move repeatedly in the closed channel constrained by fixture and workpiece and obtain a high-precision inner surface of parts under the action of micro-cutting (Petare and Jain, 2018; Jung et al., 2008).

Due to unique advantages of flexibility of AFM, many researchers have paid high attention for developing high efficient and accurate AFMs. Sato et al. (2016) took the chromium nickel-iron alloy 718 cylinders after electrical discharge machining as the research object and studied the influence of media degradation on the characteristics of AFM. The results showed that media degradation did not have much effect on surface roughness, but the material removal rate decreased exponentially. Sankar et al. (2016) proposed a rotatable AFM process and conducted experiments on AISI 4340 round tubes, the experimental results revealed the material removal rate was significantly improved, the processing time was shortened. Bremerstein et al. (2015) proposed that the increase of abrasive medium viscosity and the gradual roundness of large abrasive particles were the main factors leading to the decrease of material removal rate and surface quality. Petare et al. (2019) used laser-assisted AFM technology to finish machining spur gears. It has found that the productivity of the AFM process can be significantly improved. Ali et al. (2020) proposed the thermal additive centrifugal AFM technology, and the experimental results showed that the average material removal rate and surface finish of this technology were increased by 44.34% and 39.74%, respectively. Duval-Chaneac et al. (2018) used abrasive flow to process selective laser melted parts, which revealed the effect of abrasive flow processing medium on surface roughness and the interaction between abrasive and selective laser melted parts surface. Guo et al. (2020) analysed and experimentally studied the internal surface quality of Inconel 718 by AFM, which concluded that good surface roughness was obtained under the medium conditions of high viscosity, large particle size, low extrusion pressure, and low temperature. Liu et al. (2020) studied the relationship between abrasive hardness and erosion effect in AFM process. Through erosion experiments, it was concluded that when the ratio of abrasive hardness (Ha) and material hardness (Hm) was less than 2.6, it belonged to soft abrasive impact. When Ha/Hm > 3, it belonged to hard abrasive impact.

A digital twin analysis of combining experiment with numerical simulation is an efficient approach to understand and thus more accurately control abrasive flow processing (Mullany et al., 2017; Wiens, 2019). Li et al. (2019, 2020) used the approach of combining numerical simulation and experiment to analyse the machining mechanism of abrasive flow particles on the wall, the flow path of abrasive flow and the influence of eddy current on the wall surface of workpiece. Finally, the experimental results and numerical simulation results confirmed each other, which proved that AFM can effectively improve the surface finish of workpiece. Chih-Hua et al. (2020) studied the response of abrasives in different branch channels and concluded that the degradation of qualitative properties would affect the flow pattern distribution in the workpiece. Fu et al. (2016) proposed a new type of fixture with a guide block to perform abrasive flow processing on the integral blisk of a straight blade. It has found that a reasonably designed abrasive flow processing fixture can effectively improve the uniformity of the

blade surface finish. These achievements have demonstrated the great advantages of the digital twin-based approach in AFM with large number of uncertainties. However, the current research has not evaluated the simulation effects of various calculation models of large eddy simulation (LES).

Complex and special-shaped inner surface parts are widely used in modern engineering technology, but the above-mentioned research on this type of parts is rare. To fill this knowledge gap, a cycloid-shaped complex inner surface parts of the direct flow channel (DC) are selected as the research object in this study. By analysing the flow field distribution of AFM under different sub-grid models, the optimal sub-grid model is selected to judge the processing effect, and further machining experiments are carried out to reveal the law of abrasive flow on the surface material removal of special-shaped inner curved workpieces. The innovation of this paper is to obtain a best simulation model to guide the processing of other complex inner surfaces through mutual verification of simulation and experiment. Through simulation, the effect of abrasive flow on the workpiece is obtained. At the same time, common problems can be identified in the processing process, which includes poor processing quality of the workpiece. This method of combining simulation and experiment has been proven by many scholars to be accurate and feasible (Li et al., 2021; Singh et al., 2019; Bouland et al., 2019; Fu et al., 2019) but it is the first time to comprehensively study such different digital twin approaches in the AFM of complex shaped inner surfaces. The main contribution of this study is the comprehensive evaluation of different digital twin approaches in the AFM of complex shaped inner surfaces.

2 LES theory

During the abrasive flow processing, the fluid field exhibits a very complex turbulent state with high degree of randomness, rotations and statistics of the flow (Cinefra, 2019). LES in computational fluid dynamics (CFD) provides a more reliable means for the study of many flow mechanism problems and can be used to solve a large number of practical engineering problems, so it is chosen as the research method in this paper (Salvetti et al., 2018).

2.1 LES method

The basic idea of solving LES is to distinguish large-scale vortex from small-scale vortex through filtering operation. Among them, large-scale vortices are directly solved by the Navier-Stokes equation, and the equation is filtered to obtain the LES control equation; the small-scale vortex is solved by establishing the connection with the large-scale vortex through the sub-grid model. For the filter function and control equation used in the LES, please refer to the relevant literature for understanding (Hearing et al., 2019).

2.2 Sub-grid model

The four sub-grid models commonly used in LES includes Smagorinsky-Lilly model, wall-adapting local eddy-viscosity (WALE) model, algebraic wall-modelled large eddy

simulation (WMLES) model and dynamic kinetic energy sub-grid scale model (KET). To make comparative studies, these models are overview in this section.

2.2.1 Smagorinsky-Lilly model

According to the theory of isotropic turbulence, in the inertial sub-region, the internal energy transfer is in a local equilibrium state. Let ε be the sub-grid dissipation be $\langle 2\nu_t \overline{S}_{ij} \overline{S}_{ij} \rangle$, then:

$$\varepsilon = \left\langle \overline{S}_{ij} \tau_{ij} \right\rangle = \left\langle 2\nu_t \overline{S}_{ij} \overline{S}_{ij} \right\rangle \tag{1}$$

Use the average sub-grid eddy viscosity coefficient $\langle \nu_t \rangle$ in uniform turbulence and assume:

$$\left\langle 2\nu_t \overline{S}_{ij} \overline{S}_{ij} \right\rangle = \left\langle \nu_t \right\rangle \left\langle 2\overline{S}_{ij} \overline{S}_{ij} \right\rangle \tag{2}$$

where τ_{ij} is the sub-grid stress and $\overline{S}_{ij}$ is the strain rate tensor.

$$\varepsilon = \left\langle \nu_t \right\rangle \left\langle 2\overline{S}_{ij} \overline{S}_{ij} \right\rangle \tag{3}$$

In the isotropic turbulence, there are:

$$\left\langle 2\overline{S}_{ij} \overline{S}_{ij} \right\rangle = \int_0^{k_c} 2k^2 E(k) dk \tag{4}$$

The equilibrium energy spectrum $E(k)$ is as follows:

$$E(k) = C_k \varepsilon^{2/3} k^{-5/3} \tag{5}$$

Substituting equation (5) into equation (4), where $k_c = \pi / \Delta$, Δ is the filtering grid scale, inferred:

$$\left\langle 2\overline{S}_{ij} \overline{S}_{ij} \right\rangle = \frac{3}{2} \pi^{4/3} C_k \varepsilon^{2/3} \Delta^{-4/3} \tag{6}$$

$$\varepsilon = \frac{1}{\pi^2} \left(\frac{3}{2} C_k \right)^{-3/2} \left\langle 2\overline{S}_{ij} \overline{S}_{ij} \right\rangle^{3/2} \Delta^2 \tag{7}$$

Substituting equation (7) into equation (3):

$$\left\langle \nu_t \right\rangle = \left(C_s \Delta \right)^2 \left\langle 2\overline{S}_{ij} \overline{S}_{ij} \right\rangle^{1/2} \tag{8}$$

$$C_s = \frac{1}{\pi} \left(\frac{3}{2} C_k \right)^{-3/4} \tag{9}$$

where C_k is the Kolmogorov constant and is taken as 1.5 and $C_s = 0.18$.

2.2.2 WALE model

In this model, the eddy viscosity is defined as follows:

$$\mu_t = \rho\Delta_s^2 \frac{\left(S_{ij}^d S_{ij}^d\right)^{3/2}}{\left(\overline{S}_{ij}\overline{S}_{ij}\right)^{5/2} + \left(S_{ij}^d S_{ij}^d\right)^{5/4}} \tag{10}$$

$$\Delta_s = C_w V^{1/3} \tag{11}$$

where C_w is a constant value, which is generally 0.325. $\overline{S}_{ij}^d$ and $\overline{S}_{ij}$ respectively satisfy:

$$\overline{S}_{ij}^d = \frac{1}{2}\left(\overline{g}_{ij}^2 + \overline{g}_{ji}^2\right) - \frac{1}{3}\delta_{ij}\overline{g}_{kk}^2 \tag{12}$$

$$\overline{S}_{ij} = \frac{1}{2}\left(\frac{\partial \overline{u}_i}{\partial x_j} + \frac{\partial \overline{u}_j}{\partial x_i}\right) \tag{13}$$

$$\overline{g}_{ij} = \frac{\partial \overline{u}_i}{\partial x_j}. \tag{14}$$

2.2.3 WMLES model

The eddy viscosity is defined as:

$$\mu_t = \min\left[(kd_w)^2, \left(C_{smag}\Delta\right)^2\right] \cdot S \cdot \left\{1 - \exp\left[-\left(y^+ / 25\right)^3\right]\right\} \tag{15}$$

where d_w is the distance between the calculated point and the wall, k = 0.14, C_{smag} = 0.2, S is the speed at which it should be deformed. Where Δ is:

$$\Delta = \min\left[\max\left(C_w \cdot d_w; C_w \cdot h_{\max}; h_{wn}\right); h_{\max}\right] \tag{16}$$

where $h_{\max}$ is the maximum step size of the wall mesh and h_{wn} is the mesh step size in the normal direction of the wall, C_w = 0.15.

2.2.4 KET model

The kinetic energy sub-grid model is defined:

$$k_{sgs} = \frac{1}{2}\left(\overline{u_k^2} - \overline{u}_k^2\right) \tag{17}$$

Eddy viscosity π_t is defined as:

$$\mu_t = C_k \rho k_{sgs}^{1/2} \Delta_f \tag{18}$$

where Δ_f is the filter size.

The sub-grid stress can be written as:

$$\tau_{ij} - \frac{2}{3}\rho k_{sgs}\delta_{ij} = -2C_k \rho k_{sgs}^{1/2} \Delta_f \overline{S}_{ij} \tag{19}$$

The four sub-lattice models given in this section provide a theoretical basis for LES calculations. The key to LES is the selection of sub-lattice models, while the different

sub-lattice models adapt to different flow field requirements. The LES method is a transient solution, which can capture the transient changes of the entire flow field and obtain the maximum value of the abrasive flow during the polishing process. The different sub-grid models will obtain different numerical calculation results, thus, the next work in this paper will observe the differences and advantages between different sub-grid models and determine the appropriate sub-grid model for numerical simulation of AFM.

3 Numerical simulations

3.1 Modelling of the DC

To more accurately represent the turbulent distribution characteristics of the special-shaped surface parts processed by abrasive flow, the cycloid cross section inner surface parts of the DC were selected as the research object, and the turbulent characteristics of the flow field under the above four sub-grid models were analysed. The flow channel was extracted in three-dimensional form to visually display the internal geometry of the flow channel of the research object, in which the length of the channel was 30 mm, the cross-sectional diameter was 8 mm, and the maximum distance of the inner cavity was 5 mm. Then divided it into the structured hexahedral mesh, the inlet speed was selected as 10 m/s, the number of DC grid was 321,000 and the number of nodes was 337,183. After checked, the grid scheme meets the requirements of numerical analysis in terms accuracy and computing efficiency. A schematic diagram of DC channel can be seen in Figure 1.

3.2 Numerical analysis

Accorded to the actual solid-liquid two-phase abrasive flow processing conditions, silicon carbide particles are selected as the solid phase, which are with particle size of 300 mesh, density of 3,170 kg/m^3 and the volume fraction of 12%, and liquid phase is aviation kerosene with the density of 780 kg/m^3 and its kinematic viscosity is 6 mm^2/s. Since the inlet diameter is not a regular circle, the inlet hydraulic diameter adopted the maximum diameter of the flow channel, which is 5 mm.

Figure 1 Schematic diagram of DC channel, (a) the internal structure of the DC channel (b) cross-sectional dimensions of the DC channel (c) grid diagram of DC channel

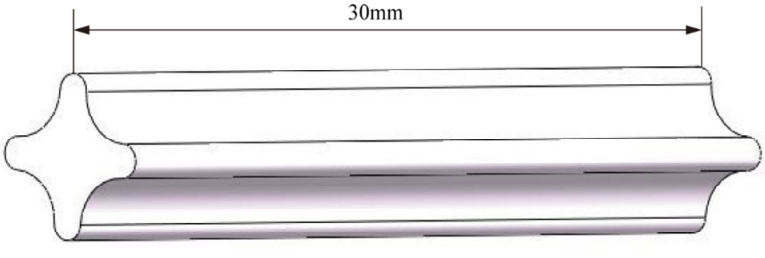

(a)

Figure 1 Schematic diagram of DC channel, (a) the internal structure of the DC channel (b) cross-sectional dimensions of the DC channel (c) grid diagram of DC channel (continued)

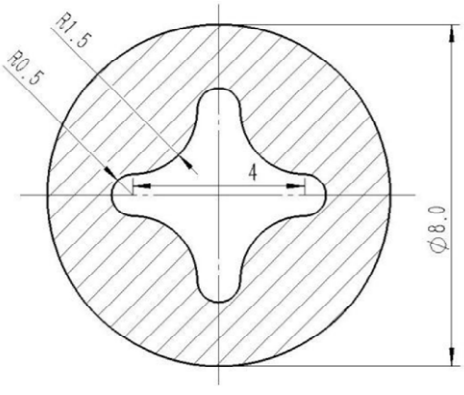

(b)

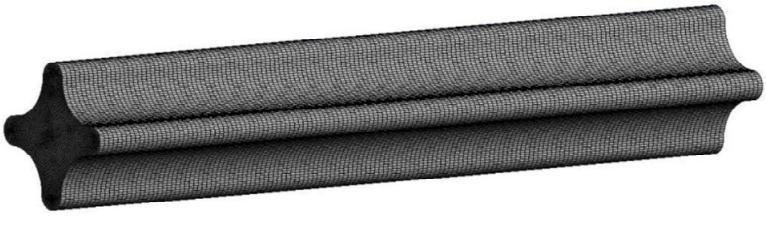

(c)

Previous studies on abrasive flow (Li et al., 2021, 2020) showed that the surface quality of the workpiece was mainly affected by the pressure difference, and the machining effect of abrasive flow was better at 2 MPa. Thus, the boundary conditions were 2 MPa at the inlet and standard atmospheric pressure at the outlet. The discrete method adopted the finite volume method, the momentum equation adopted the boundary centre difference format, the volume fraction adopted the first-order upwind style, and the transient equation adopted the second-order implicit format.

3.2.1 Static pressure analysis of AFM

As the structure of the flow channel is symmetrical, the effect of fluid on the wall surface is also symmetrical. So, half of the wall surface is based for graphics display and performance analysis. The static pressure distribution of the flow channel is shown in Figure 2. It can be seen that the lower side is the inlet, and the upper side is the outlet. The numerical results of the four sub-grid models show the same changing trend, the colour of the pipe wall change from shallow to deep, the pressure at the inlet is the highest, the pressure at the outlet is the lowest, and the pressure distribution present an obvious ladder shape, it shows that the polishing effect is from strong to weak. This is because the abrasive flow collides with the wall at the inlet, and the fluid flow carries most of the abrasive particles away from the middle of the flow channel, which gradually reduce the contact force between the abrasive flow and the wall of the workpiece.

Consequently, the abrasive flow and the wall surface cannot produce the effective friction and the collision.

Figure 2 Cloud diagram of static pressure distribution, (a) Smagorinsky model (b) WALE model (c) WMLES model (d) KET model (see online version for colours)

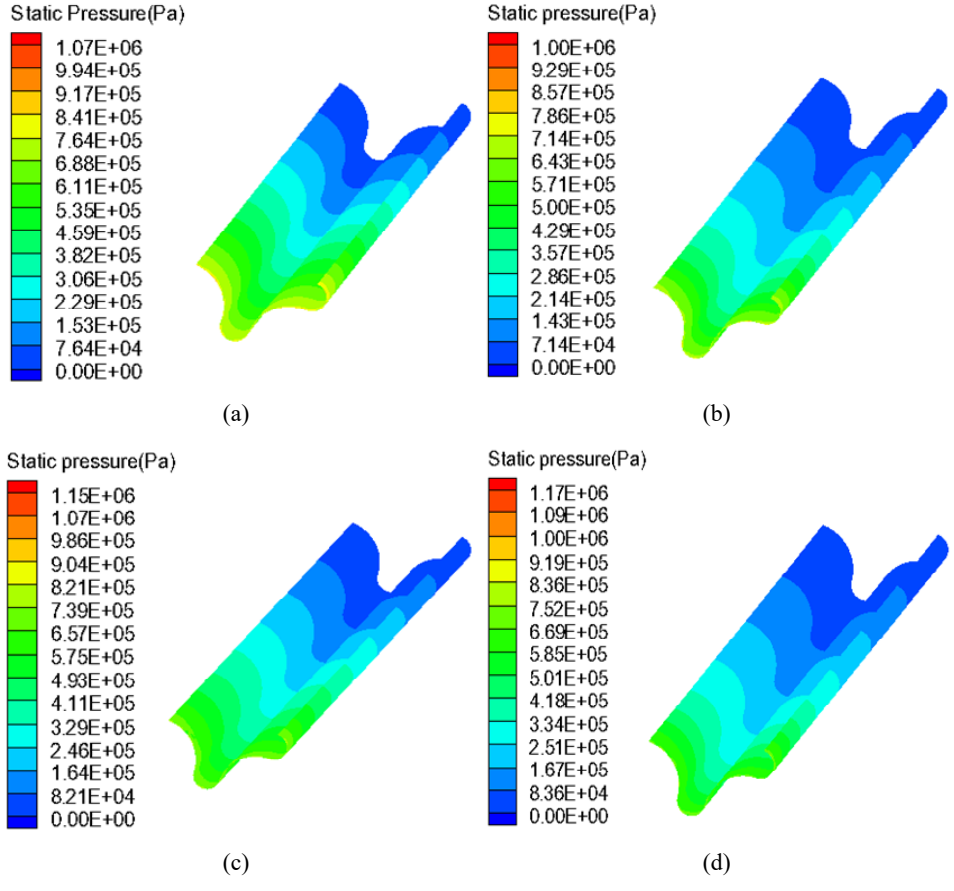

In addition, Figure 2 also reveals that different sub-grid models have different numerical calculation accuracy under the same initial conditions. From the numerical bar, it can be found that the maximum value calculated by the KET sub-grid model is 1.17 MPa, which is 9.3%, 17.0% and 1.7% larger than Smagorinsky model, WALE model and WMLES model, respectively, this shows KET model can more effectively reflect the flow behaviour. Combining with the law of AFM, the quality of the machined surface becomes better with the increase of pressure, so the KET model can be is selected for modelling and analysing the abrasive flow processing.

3.2.2 Dynamic pressure analysis of AFM

The dynamic pressure reflects a dynamic change process, the wall surface is fixed, and no change can be observed by directly observing the wall, so the middle of the flow channel was selected as the section to observe the change of internal fluid. The cross-section

diagram is shown in Figure 3, the middle section of the channel is 1–3 section, and the maximum width of the runner is 5 mm.

Figure 3 Cross-sectional position distribution

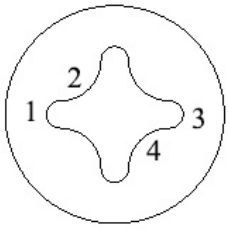

Figure 4 Cloud diagram of dynamic pressure distribution, (a) Smagorinsky model (b) WALE model (c) WMLES model (d) KET model (see online version for colours)

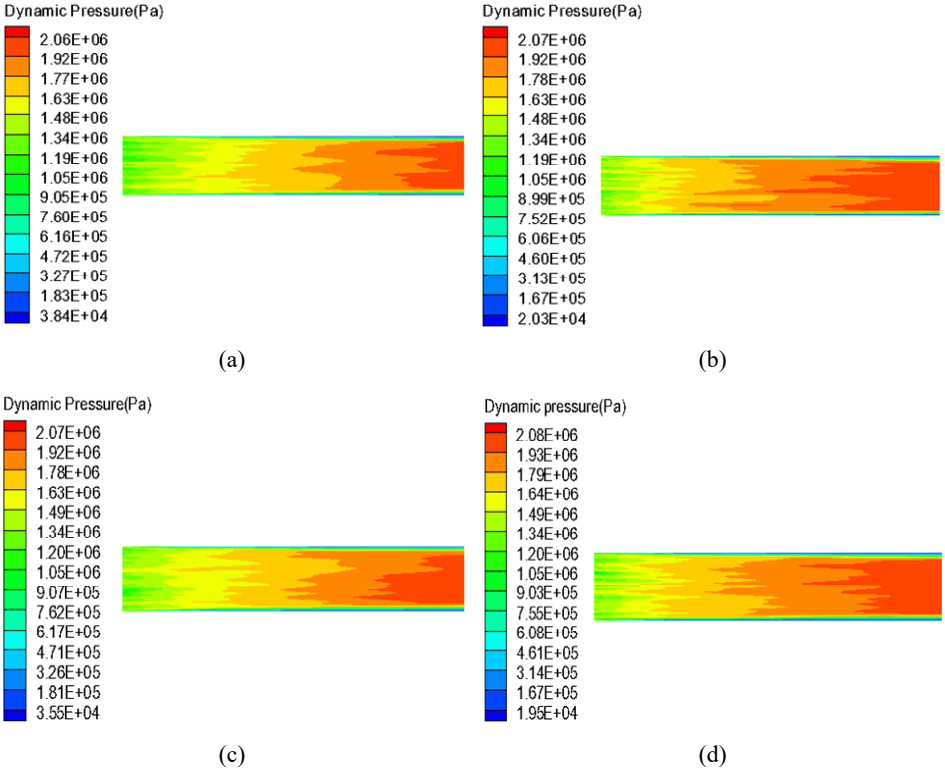

Figure 4 shows that the dynamic pressures of different models have the same changing trend. In the middle of the flow channel, the dynamic pressure is a gradually increasing process, while on the wall, the dynamic pressure decreases slowly, this changing trend and Figure 2 are mutually verified. The above occurs because the abrasive flow would inevitably collide with the wall of the workpiece when it enters the flow path. After the collision, part of the fluid kinetic energy would be lost, and part of the fluid kinetic energy would be converted into cutting energy. The abrasive flow fluid that does not

participate in the actual processing outflows from the middle flow path, and there is almost no loss of kinetic energy. Therefore, the dynamic pressure in the first half is lower than that in the second half. With the increase of the flow channel distance, the force of the abrasive flow on the wall is weakened, and the dynamic pressure at the wall gradually decreases. The polishing effect of the first half is better than the second half, which shows that the uniformity of the abrasive flow polishing on the irregular inner surface is slightly insufficient.

To facilitate the observation of the radical change of the dynamic pressure at the outlet, the dynamic pressure change curve is drawn. The abscissa is based on the upper end of the flow channel as the initial position and the lower end of the flow channel is as the endpoint. The curve change diagram is shown in Figure 5 and the wall surface can be seen that the dynamic pressure at the position is less than the dynamic pressure at the middle of the flow channel.

Figure 5 The radial dynamic pressure change curve at the outlet, (a) Smagorinsky model (b) WALE model (c) WMLES model (d) KET model

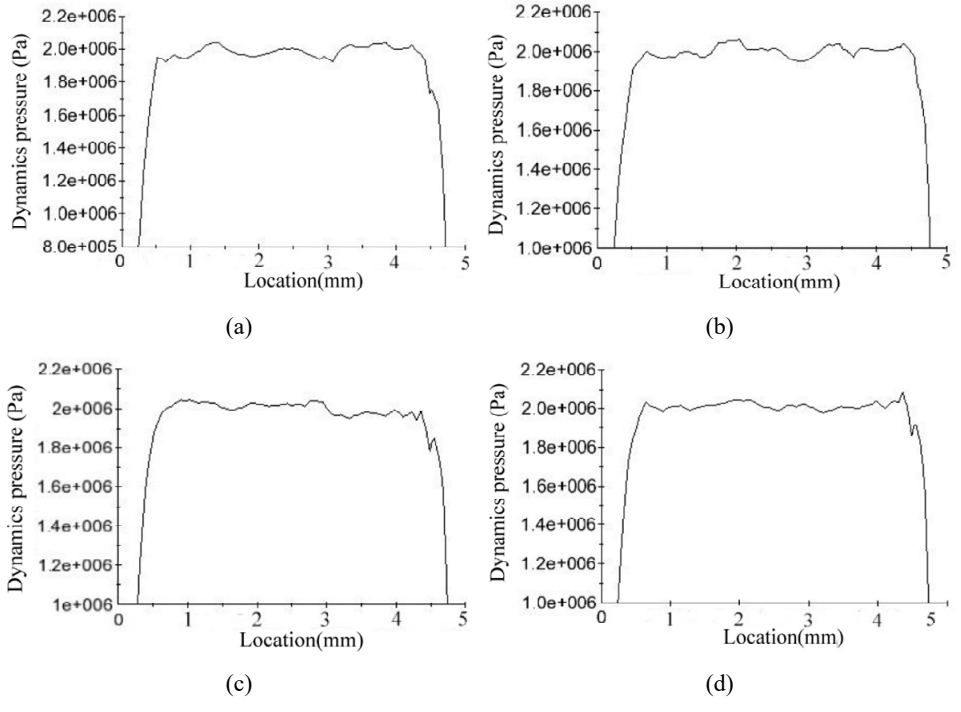

In Figures 4 and 5, the values of these models are basically identical, but there are still slight differences. The numerical result of the KET model is 2.08 MPa, which is the largest among these models. According to the influence law of abrasive flow polishing quality, the inlet pressure is proportional to the polishing quality within a certain range, the processing quality is better with the increase of pressure, so the KET model is more appropriate than others.

3.2.3 Speed and analysis of AFM

Through the velocity distribution cloud diagrams in Figure 6, it can be seen that the numerical calculations of these models are basically identical. With the increased velocity, the interaction between the abrasive flow and the wall is stronger. The greater the shear force of abrasive flow on the wall, the better the polishing quality of the inner surface of the workpiece. From the velocity distribution cloud diagram, it is found that at the inlet, the velocity decreases slightly due to the collision between the abrasive and the wall. At the outlet, the velocity in the middle of the channel is higher than that near the wall, and there is green on both sides of the red colour, which indicates that the velocity of the abrasive flow is on the same cross-section. The radial velocity at the wall decreases sharply, which is mainly due to the friction between the abrasive flow and the wall on the axial section, resulting in the decrease of the velocity. The fluid at the centre does not participate in the polishing process, and the kinetic energy loss is small.

Figure 6 The velocity distribution cloud diagram, (a) Smagorinsky model (b) WALE model (c) WMLES model (d) KET model (see online version for colours)

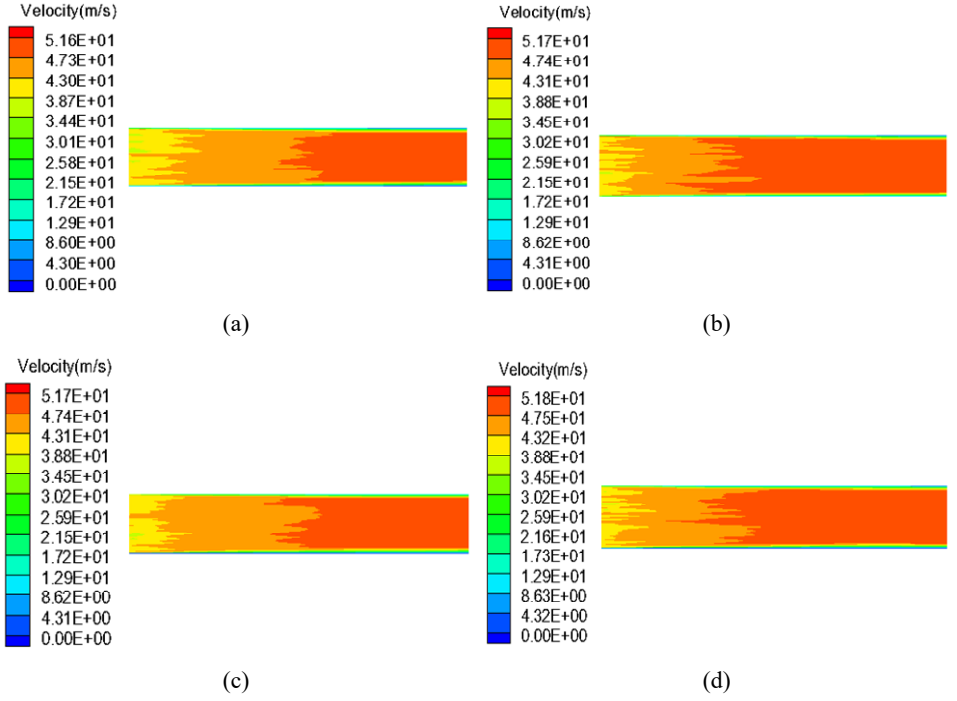

Figure 7 is the graph of the velocity distribution which shows the variation trend of outlet velocity is shown in detail, its abscissa is the same as the dynamic pressure, with the upper end of the flow path as the initial position and the lower end of the flow path as the endpoint. Compared the position of the outlet and the middle position of the flow channel, it is found that the velocity of abrasive flow decreases as the abrasive flow is closer to the wall. There is an obvious velocity difference, which indicates that there is less energy exchange between the fluid and the wall at the centre of the runner, only a small amount of kinetic energy degrades the quality of the cutting process.

Figure 7 Radial velocity change curve at the outlet, (a) Smagorinsky model (b) WALE model (c) WMLES model (d) KET model

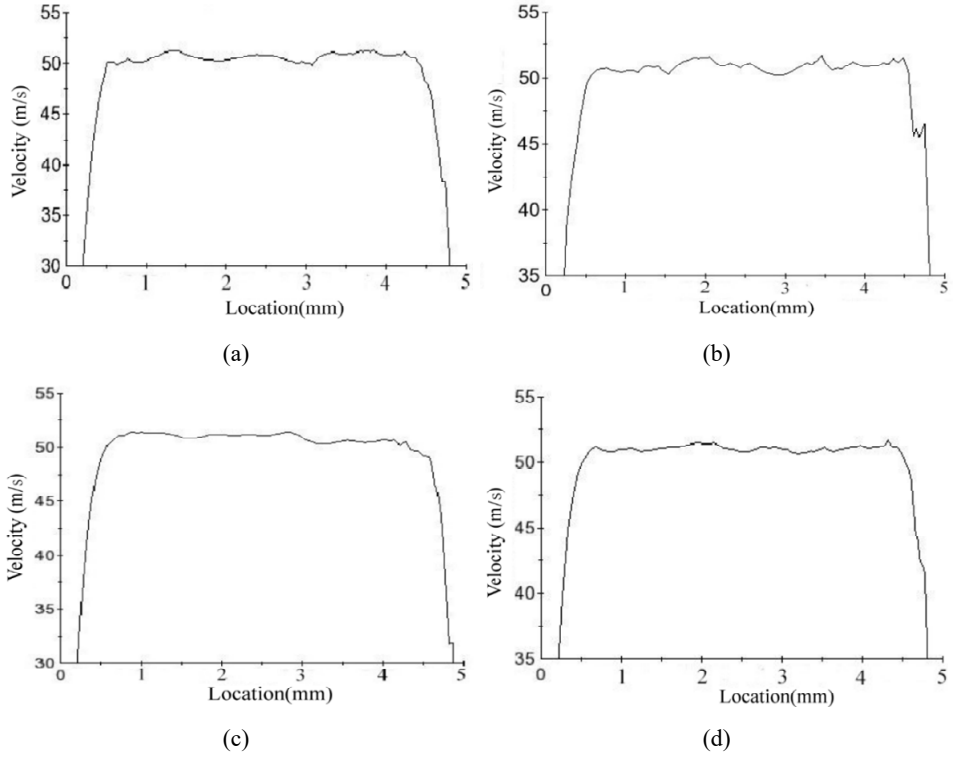

It can be seen from Figure 6 and Figure 7 that the velocity cloud distribution and the numerical value of these models are very similar, but the value of the KET model is maximal. The velocity cloud diagram shows that the red part of the WALE and KET models is earlier than the other two models, while Smagorinsky and WMLES models are slightly delayed, which show that WALE and KET models can capture small transient flow field changes with high numerical simulation accuracy.

3.2.4 Wall shear force and analysis of AFM

Through the comprehensive analysis of the above three parameters, the final consideration of the polishing effect depends on the wall shear force, which can be used to judge the numerical simulation accuracy of different sub-grid models.

Figure 8 shows that the wall shear force at the inlet is bigger than that at the outlet, and the wall shearing force becomes smaller as it moves away from the inlet, indicating that the inlet polishing effect is better than the outlet. Near the inlet, the colours of the four positions are relatively the same, indicating that the polishing effect at the inlet is relatively uniform. But in the middle and the second half of the flow channel, the wall shear force at Positions 1 and 3 is smaller than that at Positions 2 and 4, indicating that the closer to the centre of the flow channel, the greater the velocity and pressure of the fluid, which in turn reflects the abrasive flow polishing at Positions 1 and 3 is poorer than that at Positions 2 and 4.

Figure 8 Cloud diagram of wall shear force distribution, (a) Smagorinsky model (b) WALE model (c) WMLES model (d) KET model (see online version for colours)

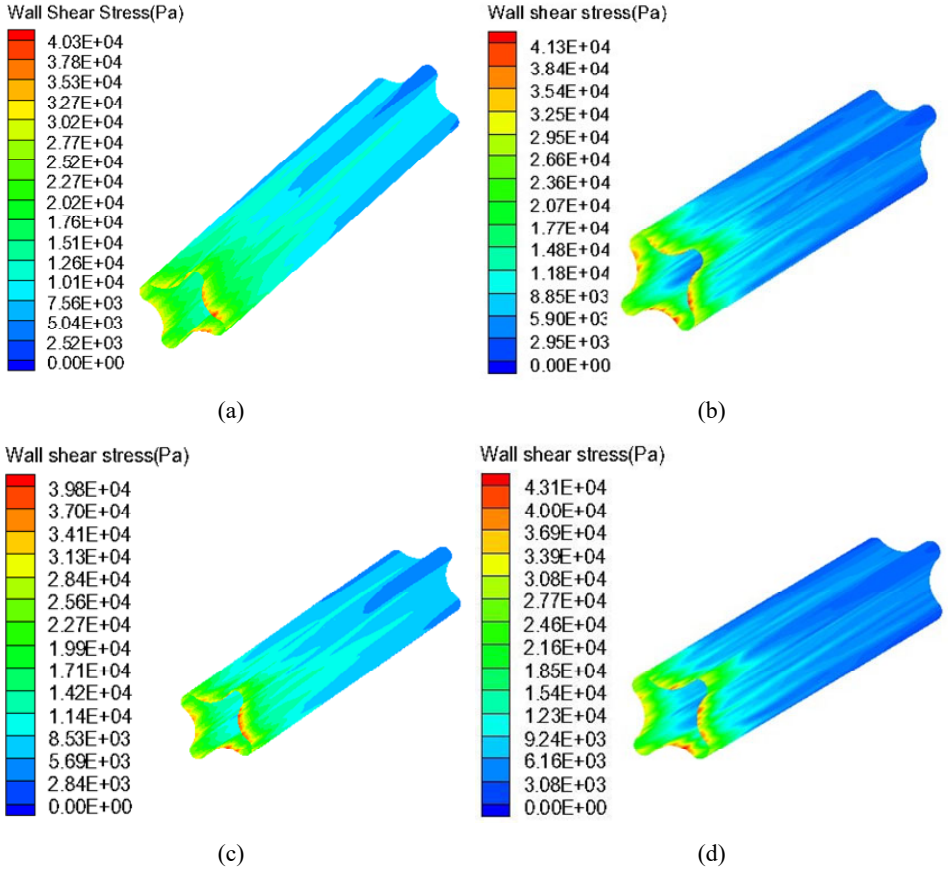

There are faults in the colour distribution on the cloud diagrams of Smagorinsky and WMLES models. The transition between different colours is very rough, and there is no gradual decrease process, indicating that the capture capabilities and simulation accuracy of the two models are poor. The colour change of WALE and KET models is relatively uniform from shallow to deep, and the transition is relatively smooth, indicating that the numerical simulation accuracy of the two models is high. It can capture the flow details of the flow field and reflect the transient motion of the fluid in real-time by WALE and KET models. But the KET model has the maximum numerical value that is consistent with the distribution of pressure, velocity and dynamic pressure.

3.2.5 Analysis of vortex and trace in AFM

The trajectory of the fluid (streamline diagram) can be analysed to reflect the fluid motion, in which the size and density of the vortex can be used to infer the kinetic energy and energy transfer at this position, thereby infers the processing effect of the position.

To facilitate the analysis of each section, the section of the flow channel is cut, and four sections are taken for analysis. The specific position and analysis are shown in Figures 9 and 10.

Figure 9 Schematic diagram of section division

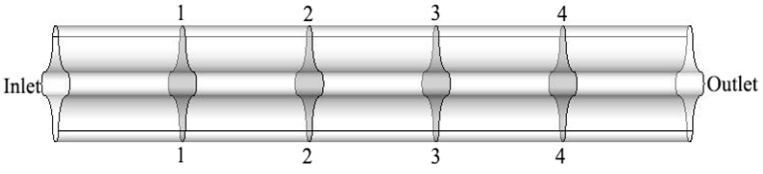

Through analysis, it founds that the distribution of vortices is basically concentrated in the middle of Positions 2 and 4, especially the large vortices, while the distributions of Positions 1 and 3 are smaller. This is because the middle of the flow channel is the mainstream area, and the large vortices can be developed. Large vortices are formed in the mainstream region, between Positions 2 and 4, and small vortices appears in four positions such as Positions 1 and 3, indicating that the fluid kinetic energy in the mainstream region is fully developed and the energy is larger. When the energy carried by the large vortex is greater, the distribution of the large vortex is greater, the kinetic energy is greater, and the processing effect on the wall is better. Therefore, the effect of fluid on Positions 2 and 4 is more obvious than that on Positions 1 and 3. From Figure 10, it can understand that the vortex distributions of the WALE and KET sub-grid models are denser, and the vortex distributions are larger than the other two sub-grid models. It shows that the WALE and KET sub-grid models have a stronger ability to capture the flow field change and simulate the dynamic change and flow details of the fluid more accurately. The simulation results of WALE and KET models have more small vortices, while the remaining two models are less distributed, indicating that the WALE and KET models grasp the weak flow of fluid more carefully and get more accurate simulation results. Through comprehensive analysis of the fluid trajectory, it concludes the WALE and KET models cannot only simulate large eddies but also simulate small eddies more accurately. The simulation accuracy of WALE and KET models is higher than that of Smagorinsky and WMLES models.

Through the comprehensive analysis of the above content, it can be seen that the KET sub-grid model has higher simulation accuracy than the other three sub-grid models, whether it is from the uniformity of the cloud diagram distribution, the size of the numerical calculation results, and the density distribution and size of the vortices. The ability to capture flow field details and weak dynamic changes is stronger, so the KET sub-grid model is more suitable for the numerical analysis of precision machining of solid-liquid two-phase abrasive flow.

Figure 10 Streamline diagram of four sub-grid models, (a) Smagorinsky model (b) WALE model (c) WMLES model (d) KET model

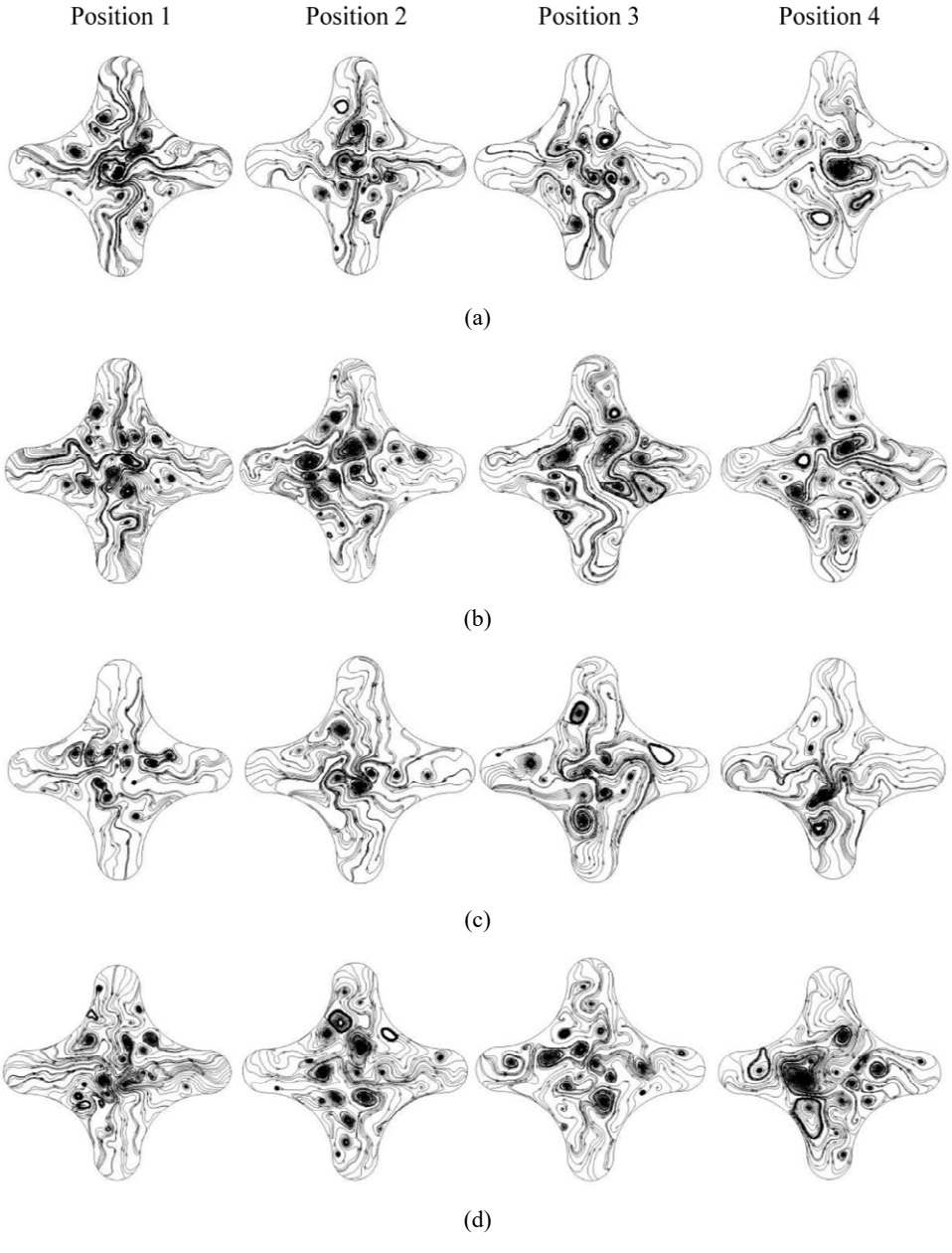

4 Experimental studies

From the numerical calculation of the DC channel with the irregular inner surface, KET model is determined to be the most suitable sub-grid model for the numerical calculation,

and the parameter distribution of the abrasive flow in the DC channel is obtained. Since our research group has simulated the machining of a special-shaped inner surface with the solid-liquid two-phase abrasive flow according to KET sub-grid model, an orthogonal test method is directly taken to explore the influence of different parameters on abrasive flow polishing quality.

The physical drawing of workpieces is illustrated in Figure 11(a). There are 10 of them in total. The first one is the original one without any machining and rest of 9 are machined with different machine parameters depicted in Tables 1 and 2. The machining was completed by the AFM shown in Figure 11(b) which can operate at maximum pressure of 6 MPa and set the predetermined polishing times.

Figure 11 Physical drawing of workpieces and abrasive flow machine, (a) physical drawing of workpieces (b) abrasive flow machine (see online version for colours)

(a)

(b)

4.1 Test procedure

According to the actual working configuration of the machine tool (Butola et al., 2018; Sankar et al., 2016; Li et al., 2020), the inlet pressure parameter is set to 2, 3 and 4 MPa. Based on previous research experience and actual experimental conditions, the polishing times are selected as 150, 200, and 250 times, and the abrasive concentration is set to be 10%, 15% and 20%. Other simulation parameters are the same as the simulation parameter settings. Subsequently, the orthogonal test with three factors and three levels is adopted in this experiment. The specific parameters are shown in Table 1, and the orthogonal test table is shown in Table 2.

Table 1 Distribution table of test parameters

Number	*Inlet pressure (MPa)*	*Polishing times (times)*	*Abrasive concentration (%)*
1	2	150	10
2	3	200	15
3	4	250	20

Table 2 Orthogonal test distribution table

Sample	*Inlet pressure (MPa)*	*Polishing times (times)*	*Abrasive concentration (%)*
01#	2	150	10
02#	2	200	15
03#	2	250	20
04#	3	150	15
05#	3	200	20
06#	3	250	10
07#	4	150	20
08#	4	200	10
09#	4	250	15

4.2 Inspection and analysis of processing test

In this experiment, silicon carbide particles with a diameter of 40 μm–50 μm are selected as the solid phase. Aviation kerosene is used as the liquid phase carrier because of its suitable density, good fluidity and thermal stability, almost no corrosion to the workpiece, high purity, and no harmful impurities, which meet the processing requirements. In addition, some additives are added according to the actual situation. Numbered the test pieces in order of sample 01# to 09#, and the original is not marked. After machined, the workpiece is placed in a sealed box with oil to avoid oxidation of the processed workpiece surface, which can affect the test results. Due to the limitation of detection method, the workpieces need to be wire-cut. After the use of wire-cutting, it is necessary to use an ultrasonic cleaning machine to remove the oil stain on the surface of the workpiece, and then clean it with absolute ethanol for detection.

4.2.1 Analysis of 3D surface profile detection

To observe the machining effect of abrasive flow on the longitudinal and transverse abrasive flow processing, four specific positions were taken for measurements and comparison, which are denoted as Positions A, B, C and D as illustrated in Figure 12. Position A is the groove of the workpiece at inlet, Position B is the arc surface at inlet, and Positions C and D are the groove and arc surface outlet, respectively. The polishing quality and surface properties are analysed at different positions after machining. The specific detection positions are shown in Figure 12.

Figure 12 Measuring positions of workpiece (see online version for colours)

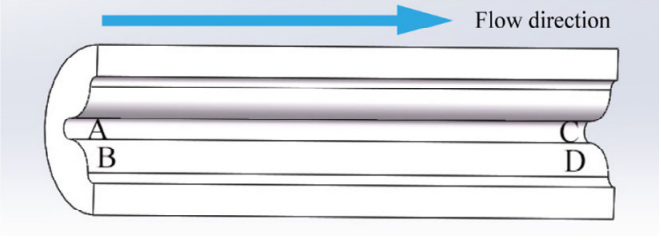

NT1100 3D surface roughness profilometer from Veeco Precision Instrument Company was used to measure the surface parameters for examining the surface quality of the workpiece, and the surface profiles of the samples 03#, 06#, and 09# were obtained. The three-dimensional surface profiles are shown in Figure 13.

It can be observed from Figure 13(a) that the surface of the workpiece is very uneven before the processing. Such surfaces with the presence of burrs and impurities not only reduce the service performance but also shorten the service life. Comparatively, samples of 03#, 06#, and 09# shown in Figures 13(b), 13(c) and 13(d) respectively show that the surface quality has improved significantly. Particularly, from different positions, the surface quality of Positions A and B is observed to be better than the other two positions. This is because Positions A and B are inlets, the collision and friction of abrasive flow at this position are more severe, and the processing effect is better. At the outlet, the kinetic energy and pressure are reduced due to the effect of abrasive flow on the wall at the inlet, and the polishing effect of abrasive flow on the outlet is weaker than that at the inlet position. What is more, it can be found that the surface roughness of Position A is slightly higher than that of Position B, and the surface roughness of Position C is greater than that of Position D. This is because the distance at Position B is closer than that of Position A, and the kinetic energy of the main flow area is greater. This proves the outstanding effectiveness of abrasive flow processing complex curved surfaces.

To sum up, the effect of abrasive flow on the longitudinal machining of the cycloid inner curved surface workpiece is better in Position B than Position A, and the horizontal machining effect of Positions A and B is better than that of Positions C and D.

4.2.2 Analysis of surface roughness

The surface contour detection can roughly display the three-dimensional shape of the surface of the workpiece, determine the material removal of the surface of the workpiece, and initially predict the processing effect of the abrasive flow. Since the test piece is a

curved part, the spot is curved when it is detected, which will cause the surface roughness to be inaccurately detected, and the obtained data result is also practical. To obtain a clear surface roughness of the DC oscillating inner curved surface, the German Mahr LD 120 stylus measuring instrument was used to detect the surface of the workpiece. Due to the detection limitations of the instrument, only Position A and Position C were measured. The surface roughness data of the workpiece before and after the abrasive flow processing is as shown in Table 3 and Figure 14.

Figure 13 Surface profile drawing, (a) surface profile before AFM (b) surface profile drawing of sample 03# (c) surface profile drawing of sample 06# (d) surface profile drawing of sample 09# (see online version for colours)

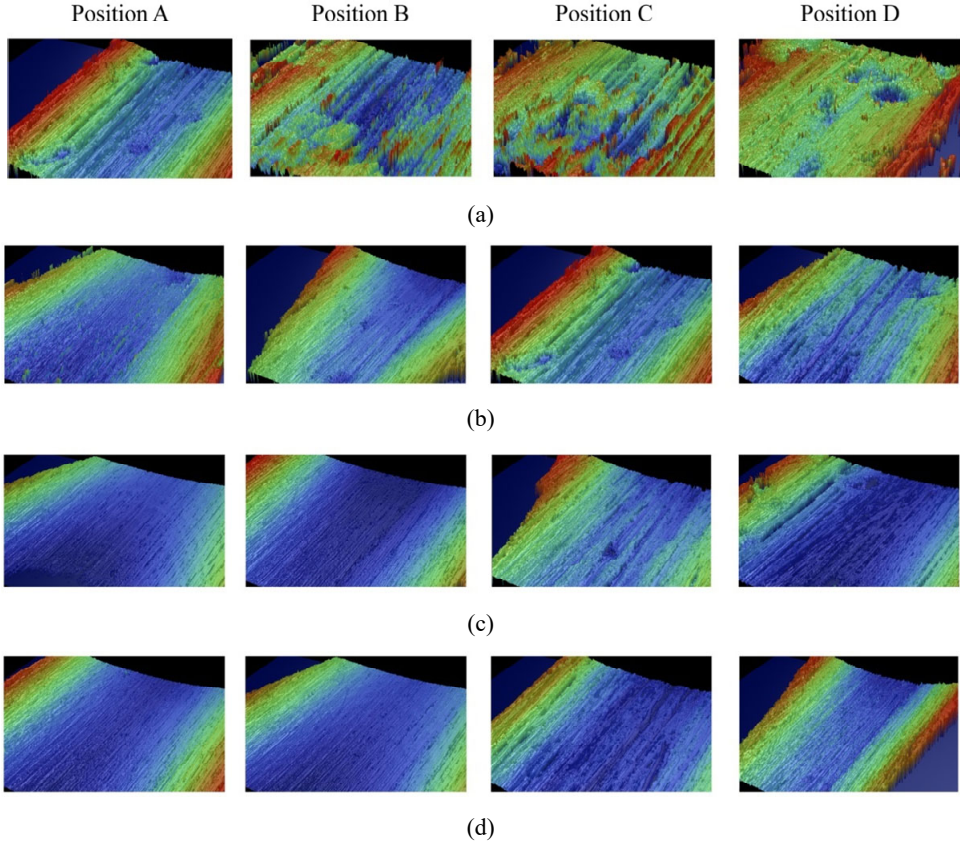

Table 3 Surface roughness Ra before and after abrasive flow processing (μm)

Position	*Original*	*01#*	*02#*	*03#*	*04#*	*05#*	*06#*	*07#*	*08#*	*09#*
Position A	1.636	0.935	0.758	0.627	0.614	0.527	0.564	0.414	0.460	0.305
Position C	1.416	1.041	0.808	0.664	0.622	0.539	0.571	0.405	0.472	0.306

After analysis, it is found that the surface roughness of the DC oscillating curved surface workpiece is large before the abrasive flow is processed, which indicates that the surface of the workpiece is not smooth, and the surface quality is poor. After the abrasive flow

processing, the surface roughness of the DC oscillating inner curved surface workpiece is significantly reduced, and the surface roughness of Positions A and C is reduced from 1.636 μm and 1.416 μm to 0.306 μm and 0.305 μm, and the surface quality is improved. The surface roughness of Position A is lower than Position C, and the detection result trend is consistent with the grating surface contour detection result. With the increase of inlet pressure, abrasive concentration and polishing times, the processing effect of the abrasive flow is gradually enhanced, which can effectively improve the surface quality. But this is not absolute. Excessive pressure will also damage the surface of the workpiece. It should be reasonably selected according to the actual processing to meet the processing requirements of the abrasive flow.

Figure 14 Surface roughness curve (see online version for colours)

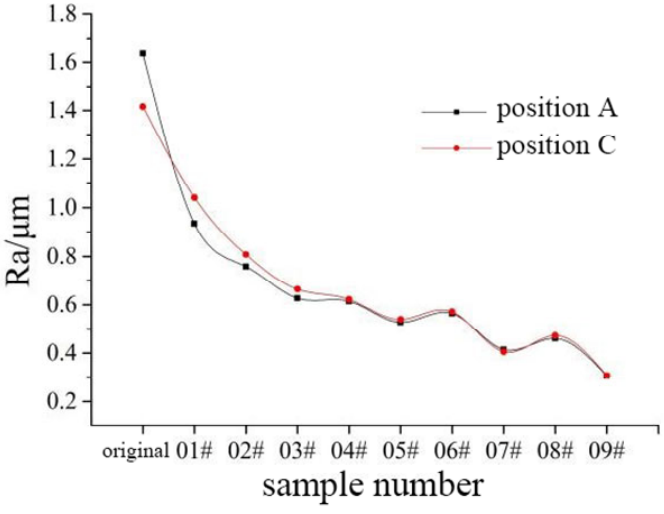

The value of Position A is smaller than the Position C, and the abrasive flow is better than the outlet for the processing at the inlet. With the increase of inlet pressure, abrasive concentration and polishing times, the surface roughness is gradually reduced, the surface quality is greatly improved, and the superiority and effectiveness of abrasive flow processing are reflected. In summary, the numerical curves from Position A and Position C show that the difference between the two decreases with the increase of inlet pressure, abrasive concentration, and polishing times. It shows that increasing the polishing parameters can improve the uniformity of the abrasive flow processing, reduce the roughness difference, and obtain better surface quality.

4.2.3 Analysis of scanning electron microscopy

To observe the surface morphology characteristics of the workpiece before and after machining, the German ZEISS EVO MA25 scanning electron microscope was taken to judge the surface morphology. The scanning electron microscope magnification is 500 times, and the detection results are shown in Figure 15.

Figure 15 Surface morphology drawing, (a)unprocessed surface morphology of the workpiece (b) surface morphology of sample 01# (c) surface morphology of sample 03# (d) surface morphology of sample 04# (e) surface morphology of sample 06# (f) surface morphology of sample 07# (g) surface morphology of sample 09#

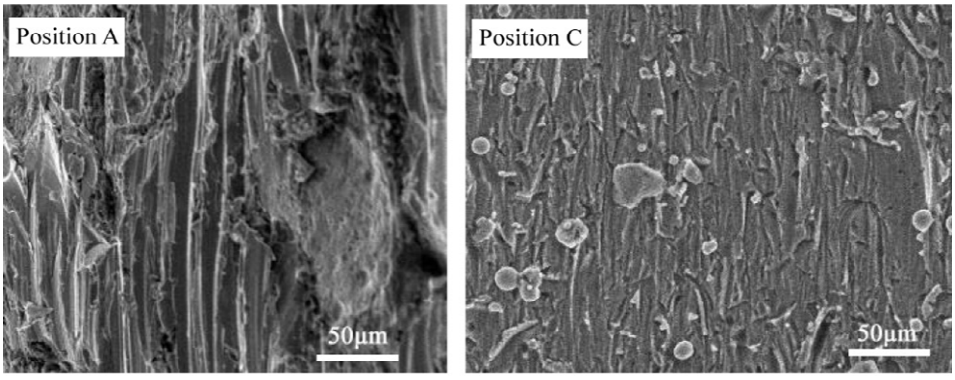

(a)

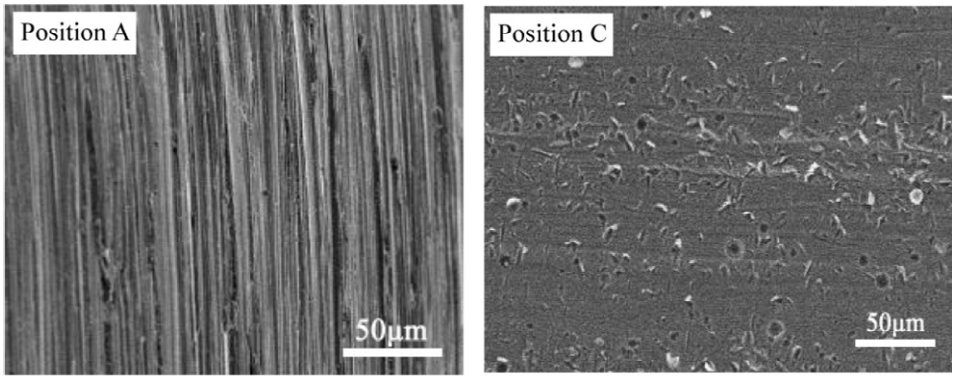

(b)

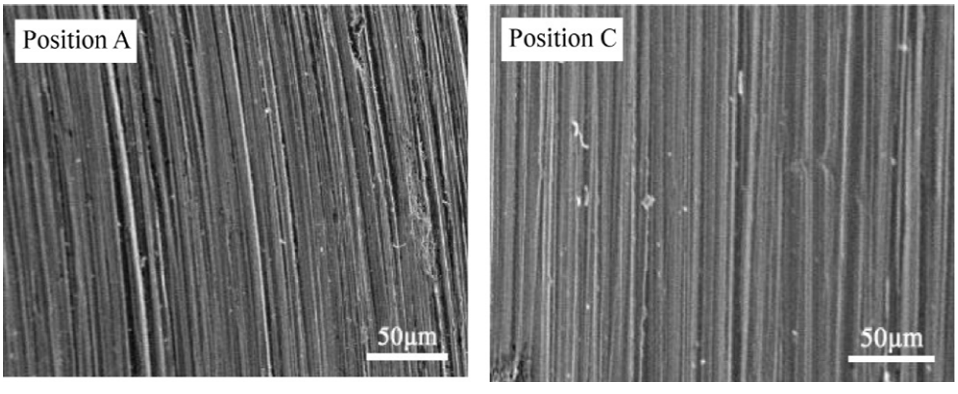

(c)

Figure 15 Surface morphology drawing, (a)unprocessed surface morphology of the workpiece (b) surface morphology of sample 01# (c) surface morphology of sample 03# (d) surface morphology of sample 04# (e) surface morphology of sample 06# (f) surface morphology of sample 07# (g) surface morphology of sample 09# (continued)

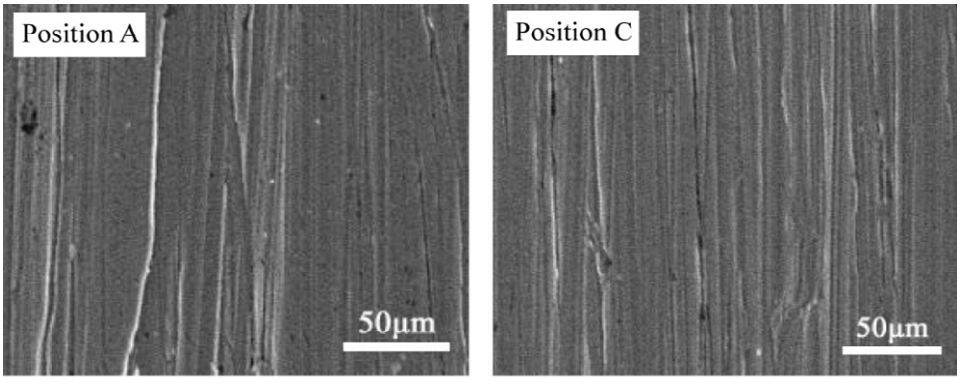

(d)

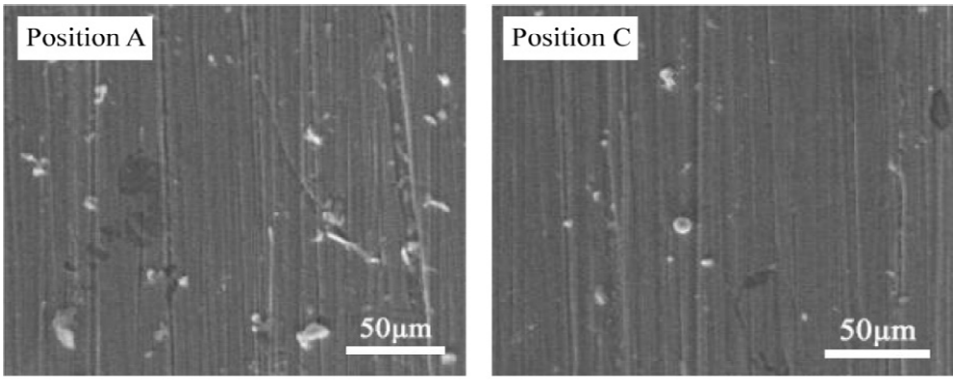

(e)

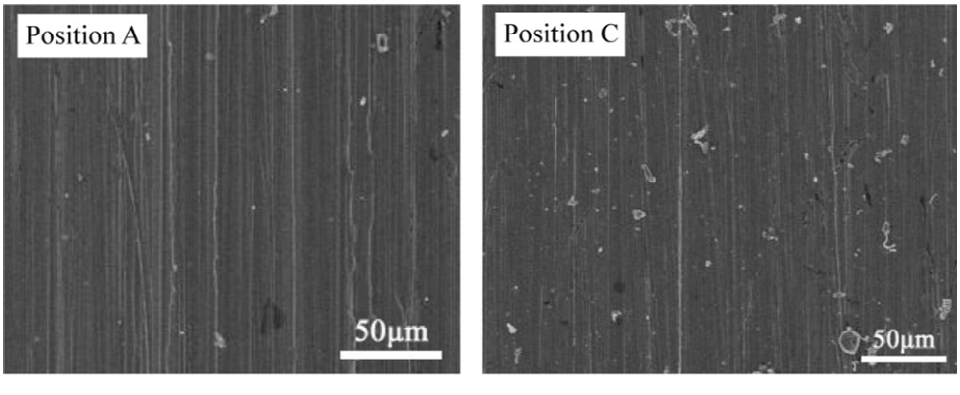

(f)

Figure 15 Surface morphology drawing, (a)unprocessed surface morphology of the workpiece (b) surface morphology of sample 01# (c) surface morphology of sample 03# (d) surface morphology of sample 04# (e) surface morphology of sample 06# (f) surface morphology of sample 07# (g) surface morphology of sample 09# (continued)

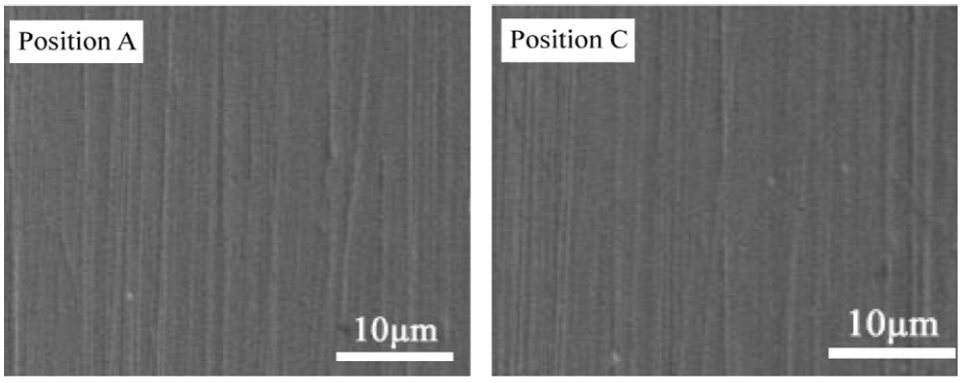

(g)

After machined, the surface morphology of the workpiece becomes smooth and flat. Some impurities, burr, pits, point, and strip protrusions on the surface are removed, and the surface quality is significantly improved. Although the surface topography has effectively improved, it can be found that the texture veins of the workpiece surface are different under different abrasive concentrations. When the abrasive concentration is 10%, the scratch on the surface of the workpiece is obvious, and with the increase of the abrasive concentration, the scratch on the surface of the workpiece gradually decreases. This is because most of the abrasives flow out of the middle of the channel during machining, when the concentration of abrasive is low, it would cause uneven particle distribution area. The particle distribution is not uniform and cannot be supplemented between different positions, and the scratch would only become more and more serious with the time, which would reduce the surface quality. With the increase of abrasive concentration, the number of particles increases, the distribution trend tends to be consistent, the force on the workpiece surface is more uniform, and the scratches are less.

4.3 Orthogonal test data analysis

Based on the surface roughness of Position A, the range analysis method and the variance analysis method were adopted to establish the orthogonal test table to determine the best parameter combination of abrasive flow polishing.

4.3.1 Orthogonal test range analysis

Accorded to the abrasive flow polishing parameters and the surface roughness obtained, the range analysis table was drawn, as shown in Table 4.

Referred the standard for determining primary and secondary factors by range A, it can be seen from Table 3 that the order of primary and secondary factors affected test indexes is $R_A > R_B > R_C$, that is, inlet pressure > polishing times > abrasive concentration, indicating that R_A is the main factor affecting surface roughness. The purpose of this test

is to obtain as low surface roughness as possible, so it needs to observe the minimum values of k_1, k_2 and k_3. Taken the inlet pressure as an example, it is observed that $k_{A3} < k_{A2} < k_{A1}$, and k_{A3} can be judged to be an excellent level. Therefore, it can be judged that k_{B3} and k_{C3} are the optimal levels of factors B and C, and the optimal level combination of A, B, and C is the optimal level combination of $A_3\underline{B}_3C_3$ for this experiment. The results show that the optimum process conditions for AFM of the workpiece are as follows: the inlet pressure is 4 MPa, the polishing times are 250, and the abrasive concentration is 15%.

Table 4 Range analysis table

Sample number	*A Inlet pressure (MPa)*	*B Polishing times (times)*	*C Abrasive concentration (%)*	*Test index Ra (μm)*
1#	2	150	10	0.935
2#	2	200	15	0.758
3#	2	250	20	0.627
4#	3	150	15	0.614
5#	3	200	20	0.527
6#	3	250	10	0.546
7#	4	150	20	0.414
8#	4	200	10	0.460
9#	4	250	15	0.305
K_{j1}	2.32	1.963	1.941	$T = \sum = 5.186$
K_{j2}	1.687	1.745	1.677	
K_{j3}	1.179	1.478	1.568	
k_{j1}	0.773	0.654	0.647	
k_{j2}	0.562	0.582	0.559	
k_{j3}	0.393	0.493	0.523	
R_i	0.380	0.161	0.124	

4.3.2 Orthogonal test variance analysis

The test data was processed by analysis of variance to obtain an analysis table of variance, as shown in Table 5.

Table 5 Analysis of variance

Source	*Freedom*	*Seq. SS*	*Adj. SS*	*Adj. MS*	*F*	*P*
Inlet pressure	2	0.217848	0.217848	0.108924	278.26	0.004
Polishing times	2	0.039338	0.039338	0.019669	50.25	0.020
Abrasive concentration	2	0.024523	0.024523	0.012261	31.32	0.031
Error	2	0.000783	0.000783	0.000391		
Total	8	0.282492				
S = 0.0197850, R-sq. = 99.72%, R-sq. (adjustment) = 98.89%						

Figure 16 The main effect diagram of each factor level and surface roughness (see online version for colours)

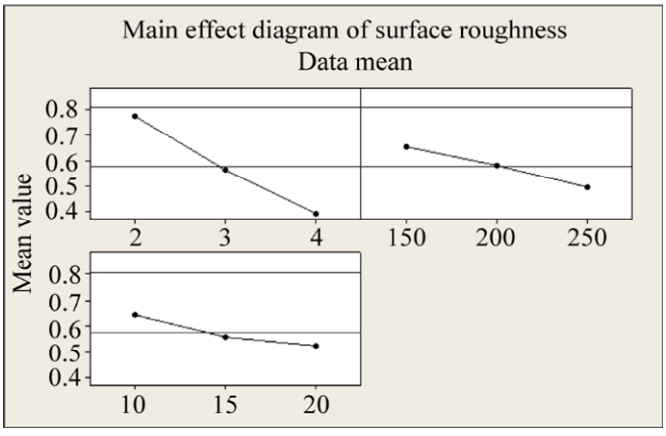

From the analysis in Table 5, it is found that the P values of inlet pressure, polishing times, and abrasive concentration are 0.004, 0.020 and 0.031, respectively. According to the value of P, the order of significance of the three factors can be judged as follows: inlet pressure > polishing times > abrasive concentration. The P values of the above factors are all less than 0.05, indicating that the main effects of the three factors are significant, and have a great influence on the surface roughness. Figure 15 shows that when the inlet pressure is 4 MPa, the polishing times is 250 and the abrasive concentration is 15%, the abrasive flow has the best polishing effect. The analysis results are consistent with the range analysis results, indicating the correctness of the above conclusions.

4.3.3 Orthogonal test regression analysis

Since the surface roughness is related to multiple variables, the relationship between roughness and variables cannot be determined. Mathematical models can be established by multiple linear regression and polynomial regression methods respectively, and the significance between the two is observed. Regression analysis is performed to determine the regression equation.

4.3.3.1 Establishment of multiple linear regression equation

Assuming that there is a linear relationship between the dependent variable y (surface roughness) and the independent variables x_1 (inlet pressure), x_2 (number of processing), and x_3 (abrasive concentration), the mathematical model is:

$$y = a_0 + a_1x_1 + a_2x_2 + a_3x_3 \tag{20}$$

After the statistical calculation of the data, the results obtained are shown in Table 6.

It can be obtained from Table 6: constant term of the regression equation is a_0 = 1.65656, the coefficient of the independent variable x_1 is a_1 = –0.19017, the coefficient of the independent variable x_2 is a_2 = –0.0016167, and the coefficient of the independent variable x_3 is a_3 = –0.01243. Through the P value of the t-test, it can be found that all P values are less than 0.05. All parameters in the formula must be present, and all three variables are significant. Thus, the regression equation can be derived as:

$$y = 1.65656 - 0.19017x_1 - 0.0016167x_2 - 0.012433x_3 \quad (21)$$

Table 6 Regression parameter table

Independent variable	*Coefficient*	*Coefficient standard deviation*	*T*	*P*
Constant	1.65656	0.06004	27.59	0.000
Inlet pressure	–0.19017	0.01020	–18.65	0.000
Polishing times	–0.0016167	0.0002039	–7.93	0.001
Abrasive concentration	–0.012433	0.002039	–6.10	0.002
S = 0.0249762, R-sq. = 98.9%, R-sq. (adjustment) = 98.2%				

After obtaining the regression equation, it needs to be tested for significance, and the F test is applied here. The test results are shown in Table 7. The P value is less than 0.05, indicating that the regression equation is valid.

Table 7 Test table

Source	*Degree of freedom*	*SS*	*MS*	*F*	*P*
Return	3	0.279373	0.093124	149.28	0.000
Residual error	5	0.003119	0.000624		
Total	8	0.282492			

Figure 17 Roughness residual diagram (see online version for colours)

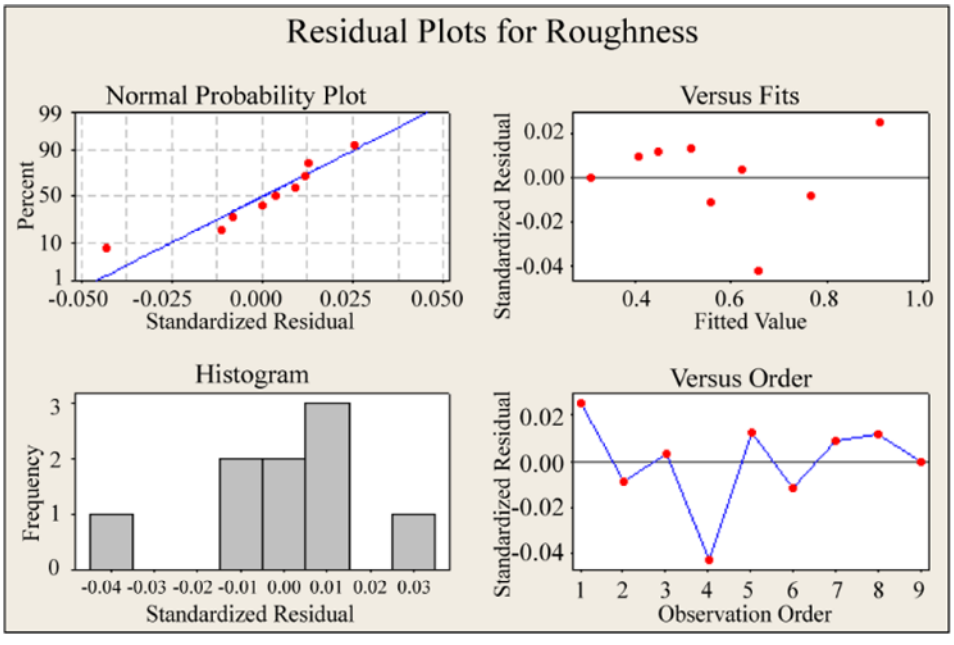

The regression model is appropriate by residual analysis. The whole result is incomplete from the variance analysis table and the coefficient test analysis. The result of the judgement is shown in Figure 17 and Figure 18.

Figure 18 Scatter plot between residual and respective variables, (a) residual and inlet pressure (b) residual and polishing times (c) residual and abrasive concentration (see online version for colours)

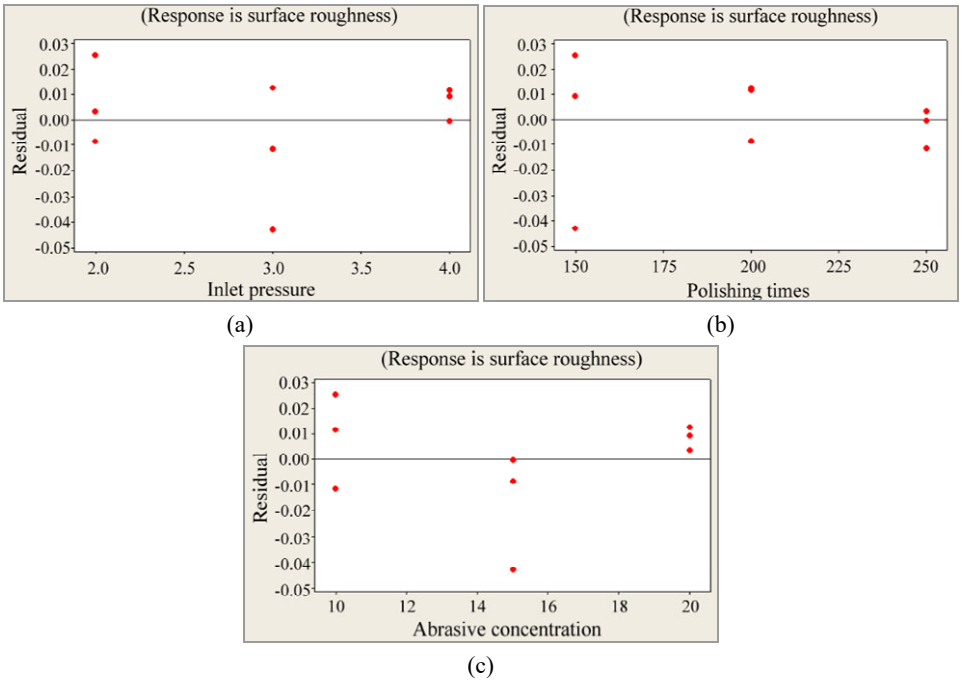

Figure 17 is mainly to observe whether the residual is normally distributed, and whether the points in the sequential scatter plot fluctuate randomly on the horizontal axis, and whether the fitted value has a 'flare' or 'funnel shape'. Figure 18 focuses on whether there is a tendency to bend, in the results of this test, the figures are normal, and there is no obvious tendency to bend.

The residual is by the normal distribution, and the fitting value in the upper right corner is normal, and the order in the lower right corner also conforms to the changing trend. Therefore, the regression equation is consistent with this test, and there is no large deviation, which proves that the regression equation is reasonable.

4.3.3.2 Establishment of a polynomial regression equation

Assume that the relationship between the dependent variable y (surface roughness) and the independent variables x_1 (inlet pressure), x_2 (number of processing), and x_3 (abrasive concentration) is a nonlinear function. Since the independent variables are three, a ternary cubic polynomial regression equation is established, as follows:

$$\begin{aligned} y = {} & a_0 + a_1x_1 + a_2x_2 + a_3x_3 + a_4x_1x_2 + a_5x_1x_3 + a_6x_2x_3 + a_7x_1^2 + a_8x_2^2 \\ & + a_9x_3^2 + a_{10}x_1x_2x_3 + a_{11}x_1^2x_2 + a_{12}x_1^2x_2 + a_{13}x_2^2x_3 + a_{14}x_1x_2^2 + a_{15}x_1x_3^2 \\ & + a_{16}x_2x_3^2 + a_{17}x_1^3 + a_{18}x_2^3 + a_{19}x_3^3 \end{aligned} \tag{22}$$

Let $z_1 = x_1, z_2 = x_2, z_3 = x_3, z_4 = x_1x_2, \ldots\ldots, z_{19} = x_3^3$, and this translates into a 19-element linear regression equation:

$$y = a_0 + a_1 z_1 + a_2 z_2 + a_3 z_3 + a_4 z_4 + a_5 z_5 + a_6 z_6 + \ldots\ldots + a_{19} z_{19} \tag{23}$$

Since there are 19 independent variables, it is not conducive to parameter optimisation. Therefore, the stepwise regression method is used to screen the independent variables, and then the multiple linear regression analysis is performed according to the screening results. The stepwise regression calculation results are obtained as shown in Table 8.

Table 8 Stepwise regression table

Step	*1*	*2*
Constant	0.8602	1.1252
z_{11}	–0.00015	–0.00015
T value	–5.31	–10.09
P value	0.001	0.000
z_3		–0.0168
T value		–4.17
P value		0.006
S	0.0896	0.0490
R-sq.	80.10	94.89
R-sq. (adjustment)	77.25	93.19

Result analysis: there are 1 and 2 after the step. After the step, there are two steps to filter the factor. The variables selected are z_{11} and z_3, that is $x_1^2 x_2$ and x_3, so you can get the regression equation:

$$y = 1.1252 - 0.0168 x_3 - 0.00015 x_1^2 x_2 \tag{24}$$

Then, according to the selected independent variables, regression analysis is performed as shown in Table 9.

Table 9 Regression parameter table

Independent variable	*Coefficient*	*Coefficient standard deviation*	*T*	*P*
Constant	1.12521	0.07187	15.66	0.000
$x_1^2 x_2$	–0.00015371	0.00001523	–10.09	0.000
x_3	–0.016788	0.004028	–4.17	0.006
S = 0.0490435, R-sq. = 94.9%, R-sq. (adjustment) = 93.2%				

From the last column of Table 9, it can be found that all the 'P' values of the t-test performed on the three parameters are less than 0.05. It is proved that all the items in the formula are significant, and the regression equation is also available. But from the regression model error as a percentage of the total error (R-sq.), the R-sq. of the polynomial regression is 94.9%, while the R-sq. of the multiple linear regression is 98.9% shown in Table 6. The larger the value, the better the regression model and the data agree, indicating that the regression equation obtained by multiple linear regression has a better fit with the experimental data.

5 Conclusions

This paper discusses the ability of four sub-lattice models to capture the turbulence characteristics of the flow channel when the irregular curved inner channel is processed by the abrasive flow, and the machining experiments are carried out with numerical analysis. The following conclusions are drawn:

1 Analysing the turbulence characteristics of the flow field under the four sub-grid models of Smagorinsky, WALE, WMLES and KET, it can be found that the middle part of the flow channel is the mainstream area, where the large vortices are concentrated, and the processing effect on the workpiece wall is better than other small vortices. The KET model can effectively capture the minute details of the flow field and the transient flow field changes, clearly distinguish the density and size of the vortex, and have high numerical calculation accuracy.

2 The experimental results of AFM show that the surface quality of the cycloidal inner surface workpiece with the DC has been significantly improved, and the surface roughness is reduced from 1.635 μm to 0.305 μm. The surface quality at the inlet is better than that at the outlet, and the two-way machining can help solve the problem of inconsistent processing quality.

3 The closer the wall is to the centre of the flow channel, the greater the force, and the better the precision machining quality of abrasive flow. Through the range analysis and variance analysis of the experimental data, it is found that the order of significance of the factors affecting AFM is as follows: inlet pressure > polishing times > abrasive concentration. The best combination of parameters for AFM of irregular inner surface is as follows: inlet pressure is 4 MPa, polishing times is 250 times and abrasive concentration is 15%.

References

Ali, P., Walia, R.S., Murtaza, Q. et al. (2020) 'Material removal analysis of hybrid EDM-assisted centrifugal abrasive flow machining process for performance enhancement', *Journal of the Brazilian Society of Mechanical Sciences and Engineering*, Vol. 42, No. 6, pp.1–28.

Bouland, C., Urlea, V., Beaubier, K. et al. (2019) 'Abrasive flow machining of laser powder bed-fused parts: numerical modeling and experimental validation', *Journal of Materials Processing Technology*, Vol. 273, p.116262.

Bremerstein, T., Potthoff, A., Michaelis, A. et al. (2015) 'Wear of abrasive media and its effect on abrasive flow machining results', *Wear*, Vol. 342, pp.44–51.

Butola, R., Jain, R., Bhangadia, P. et al. (2018) 'Optimization to the parameters of abrasive flow machining by Taguchi method', *Materials Today: Proceedings*, Vol. 5, No. 2, pp.4720–4729.

Cheema, M.S., Venkatesh, G., Dvivedi, A. et al. (2012) 'Developments in abrasive flow machining: a review on experimental investigations using abrasive flow machining variants and media', *Proceedings of the Institution of Mechanical Engineers Part B – Journal of Engineering Manufacture*, Vol. 226, No. 12, pp.1951–1962.

Chih-Hua, W., Wai, K.C., Ming, W.S.Y. et al. (2020) 'Numerical and experimental investigation of abrasive flow machining of branching channels', *The International Journal of Advanced Manufacturing Technology*, Vol. 108, No. 9, pp.2945–2966.

Cinefra, M. (2019) 'Hydro-mechanical analysis of pipe armed by nanoparticles based on numerical methods', *International Journal of Hydromechatronics*, Vol. 2, No. 3, pp.247–259.

Duval-Chaneac, M.S., Han, S., Claudin, C. et al. (2018) 'Experimental study on finishing of internal laser melting (SLM) surface with abrasive flow machining (AFM)', *Precision Engineering*, Vol. 54, pp.1–6.

Fu, Y., Gao, H., Yan, Q. et al. (2019) 'A new predictive method of the finished surface profile in abrasive flow machining process', *Precision Engineering*, Vol. 60, pp.497–505.

Fu, Y., Wang, X., Gao, H. et al. (2016) 'Blade surface uniformity of blisk finished by abrasive flow machining', *The International Journal of Advanced Manufacturing Technology*, Vol. 84, Nos. 5–8, pp.1725–1735.

Guo, J., Song, C., Fu, Y. et al. (2020) 'Internal surface quality enhancement of selective laser melted Inconel 718 by abrasive flow machining', *Journal of Manufacturing Science and Engineering*, Vol. 142, No. 10, p.101003.

Hearing, S.W., Lee, M. and Moser, R.D. (2019) 'Resolution-induced anisotropy in large-eddy simulations', *Physical Review Fluids*, Vol. 4, No. 11, pp.114605.

Jung, D., Wang, W.L., Knafl, A. et al. (2008) 'Experimental investigation of abrasive flow machining effects on injector nozzle geometries, engine performance, and emissions in a DI diesel engine', *International Journal of Automotive Technology*, Vol. 9, No. 1, pp.9–15.

Kum, C.W., Wu, C.H., Wan, S. et al. (2020) 'Prediction and compensation of material removal for abrasive flow machining of additively manufactured metal components', *Journal of Materials Processing Technology*, Vol. 282, pp.116704.

Li, J., Dong, X., Liu, Y. et al. (2021) 'Quality research and prediction of six-order variable-diameter pipe processed by solid-liquid two-phase magnetic abrasive flow', *The International Journal of Advanced Manufacturing Technology*, Vol. 114, No. 11, pp.3763–3778.

Li, J., Zhang, H., Wei, L. et al. (2019) 'Formation mechanism and quality control technology for abrasive flow precision polishing vortex: large eddy simulation', *The International Journal of Advanced Manufacturing Technology*, Vol. 105, No. 5, pp.2135–2150.

Li, J., Zhu, Z., Wang, B. et al. (2020) 'Elbow precision machining technology by abrasive flow based on direct Monte Carlo method', *Journal of Central South University*, Vol. 27, No. 12, pp.3667–3683.

Liu, Y., Chen, C., Wei, J. et al. (2020) 'Influence of abrasive hardness on erosion wear of abrasive air jets', *Journal of Central South University*, Vol. 27, No. 2, pp.356–371.

Mali, H.S. and Manna, A. (2009) 'Current status and application of abrasive flow finishing processes: a review', *Proceedings of the Institution of Mechanical Engineers Part B – Journal of Engineering Manufacture*, Vol. 223, No. 7, pp.809–820.

Mullany, B., Shahinian, H., Navare, J. et al. (2017) 'The application of computational fluid dynamics to vibratory finishing processes', *CIRP Annals*, Vol. 66, No. 1, pp.309–312.

Petare, A.C. and Jain, N.K. (2018) 'A critical review of past research and advances in abrasive flow finishing process', *The International Journal of Advanced Manufacturing Technology*, Vol. 97, No. 1, pp.741–782.

Petare, A.C., Mishra, A., Palani, I.A. et al. (2019) 'Study of laser texturing assisted abrasive flow finishing for enhancing surface quality and microgeometry of spur gears', *The International Journal of Advanced Manufacturing Technology*, Vol. 101, No. 1, pp.785–799.

Salvetti, M.V., Fröhlich, J., Geurts, B.J. et al. (2018) 'Direct and large eddy simulation', *Flow, Turbulence and Combustion*, Vol. 101, No. 2, pp.269–270.

Sambharia, J. and Mali, H.S. (2019) 'Experimental study on charging performance and spray characteristics of induction charged spray', *Proceedings of the Institution of Mechanical Engineers Part B – Journal of Engineering Manufacture*, Vol. 233, No. 2, pp.388–399.

Sankar, M.R., Jain, V.K. and Ramkumar, J. (2016) 'Nano-finishing of cylindrical hard steel tubes using rotational abrasive flow finishing (R-AFF) process', *The International Journal of Advanced Manufacturing Technology*, Vol. 85, No. 9, pp.2179–2187.

Sato, T., Soh, E., Nakayama, Y. et al. (2016) 'Effect of media degradation on finishing characteristics in abrasive flow machining', *Materials Science Forum*, Vol. 874, pp.127–132.

Singh, S., Kumar, D., Sankar, M.R. et al. (2019) 'Viscoelastic medium modeling and surface roughness simulation of microholes finished by abrasive flow finishing process', *The International Journal of Advanced Manufacturing Technology*, Vol. 100, No. 5, pp.1165–1182.

Wiens. T. (2019) 'Engine speed reduction for hydraulic machinery using predictive algorithms', *International Journal of Hydromechatronics*, Vol. 2, No. 1, pp.16–31.